SCIENCE CHINA
Information Sciences

• RESEARCH PAPER •
Special Focus on Millimeter Wave Communications Techniques and Devices for 5G

August 2017, Vol. 60 080305:1–080305:12
doi: 10.1007/s11432-017-9139-4

A novel 3D frequency domain SAGE algorithm with applications to parameter estimation in mmWave massive MIMO indoor channels

Rui FENG[1], Jie HUANG[1], Jian SUN[1,2*] & Cheng-Xiang WANG[3,1]

[1]*Shandong Provincial Key Laboratory of Wireless Communication Technologies, Shandong University, Jinan* 250100*, China;*
[2]*State Key Laboratory of Millimeter Waves, Southeast University, Nanjing* 210096*, China;*
[3]*Institute of Sensors, Signals and Systems, School of Engineering & Physical Sciences, Heriot-Watt University, Edinburgh* EH14 4AS*, UK*

Received May 9, 2017; accepted June 13, 2017; published online July 5, 2017

Abstract Millimeter wave (mmWave) and massive multiple-input multiple-output (MIMO) wireless communication channels show some new characteristics different from conventional channels. In order to have an in-depth understanding of mmWave massive MIMO channels, we conduct channel measurements at 16, 28, and 38 GHz frequency bands using virtual large horizontal planar arrays in an indoor office environment. First, a three dimensional (3D) frequency domain (FD) parameter estimation algorithm extended from the space alternating generalized expectation-maximization (SAGE) algorithm is proposed and used to process the measurement data. Second, by dividing the large array into several sub-arrays and calculating power delay profiles (PDPs), power azimuth angle profiles (PAAPs), and power elevation angle profiles (PEAPs), we analyze the changes of delay, azimuth angle of arrival (AAoA), and elevation AoA (EAoA) over the large array. We find that the spatial cross-correlation functions (SCCFs) calculated along different directions of the planar array exhibit significant variations. Third, the comparison of the averaged PDPs (APDPs) at three different frequency bands shows that the attenuation increases when mmWave channels move to high frequency bands. Furthermore, SCCFs of channels at three frequency bands are also compared for two uniform linear arrays (ULAs). We draw conclusion that the correlation coefficients can be affected by not only measurement environments, but also the relative angle between transmitter (Tx) pointing direction and receiver (Rx) large array, and the operating frequency bands.

Keywords millimeter wave bands, massive MIMO, 3D FD-SAGE algorithm, planar array, statistical properties

Citation Feng R, Huang J, Sun J, et al. A novel 3D frequency domain SAGE algorithm with applications to parameter estimation in mmWave massive MIMO indoor channels. Sci China Inf Sci, 2017, 60(8): 080305, doi: 10.1007/s11432-017-9139-4

* Corresponding author (email: sunjian@sdu.edu.cn)

1 Introduction

Stimulated by the exploding requirements of wireless communications for human and device connections, the fifth generation (5G) wireless communication system aims to have a dramatic improvement in capacity, energy and spectral efficiency, and data rate compared with the fourth generation (4G) system [1,2]. It incorporates several new technologies to fulfill the blueprint, such as millimeter wave (mmWave) communications, massive multiple-input multiple-output (MIMO), green communications, etc. [2]. However, the employment of new techniques brings new propagation characteristics into the underlying channels. The mmWave frequency band can provide larger bandwidth to support Gigabits per second (Gbps) transmission data rate and higher time resolution than conventional frequency bands. But the transmitted signal will suffer more severe attenuation [3]. Massive MIMO channels may exhibit new characteristics like spherical wavefront and non-stationarity in space domain [4,5]. In addition, it was pointed out in [6] that mmWave and massive MIMO could be complemented with respect to the antenna array size and cell coverage. This is because massive MIMO with beamforming (BF) technique can compensate the high attenuation of mmWave channels and mmWave enables the reduction of massive MIMO array size.

To have a better understanding of wireless channels, channel measurements and modeling should be conducted. One key step here is to use high resolution parameter estimation algorithms to extract the path parameters from the measurement data and further analyze channel characteristics. These parameters include complex amplitude, delay, azimuth angle of departure (AAoD), elevation AoD (EAoD), azimuth angle of arrival (AAoA), elevation AoA (EAoA), and Doppler shift, etc. In array signal processing, there are mainly three kinds of estimation methods, i.e., spectral estimation, parametric subspace-based estimation, and deterministic parametric estimation [7]. The former two kinds of algorithms perform far from satisfactory for estimating highly correlated multipath components (MPCs). Within the third category are the expectation-maximization (EM) and space alternating generalized expectation-maximization (SAGE) algorithms. SAGE algorithm is an extension of EM algorithm by dividing all parameters into several subsets in the maximization step and is capable of the joint estimation of those parameters in time domain [8]. For channel measurements carried out in frequency domain using a vector network analyzer (VNA), it is more convenient to process the measurement data in frequency domain based sounder. In [9], a frequency domain (FD) SAGE algorithm was introduced to estimate delay, AAoA, and complex amplitude jointly. It was further extended to the MIMO case in [10] to extract directional information at both ends of the radio link. However, it was confined to the estimation of azimuth angles. In this paper, a three dimensional (3D) FD-SAGE algorithm that can be used to estimate azimuth and elevation angles at both Tx and Rx sides is presented [11].

Researchers have already carried out extensive mmWave channels and massive MIMO channel measurements. However, massive MIMO channel measurements are often carried out at frequency band below 6 GHz, and mmWave channel measurements are usually configured with horn antenna or conventional MIMO antenna array. The researchers at Lund University conducted some massive MIMO channel measurements at 2.6 GHz using a virtual 128-element uniform linear array (ULA) and a 128-element cylindrical array. They focused on studying the condition number and sum-rate capacity of the channel and the capability of large array to separate closely spaced users [12], and found out that the near field effect and the non-stationarity over the array helped decorrelating the channels of different users [13]. In [14], channel measurements carried out at 28 and 38 GHz in urban environments were introduced. The receive (Rx) antenna was swept 360° in azimuth plane with 10° steps. MmWave massive MIMO channel measurements in a typical office environment using massive antenna array at four mmWave frequency bands, i.e., 11, 16, 28, and 38 GHz, were carried out and analyzed in [15]. Statistical properties such as delay spread and angle spread and new massive MIMO propagation properties were compared at the four frequency bands, where a 3D time domain SAGE algorithm was used. To the best of our knowledge, channel statistical properties like power delay profile (PDP), power azimuth angle profile (PAAP), power elevation angle profile (PEAP), and spatial cross-correlation functions (SCCFs) along different dimensions of a large planar or cube array at mmWave frequency bands have never been compared before.

The major contributions of this work are summarized as follows:

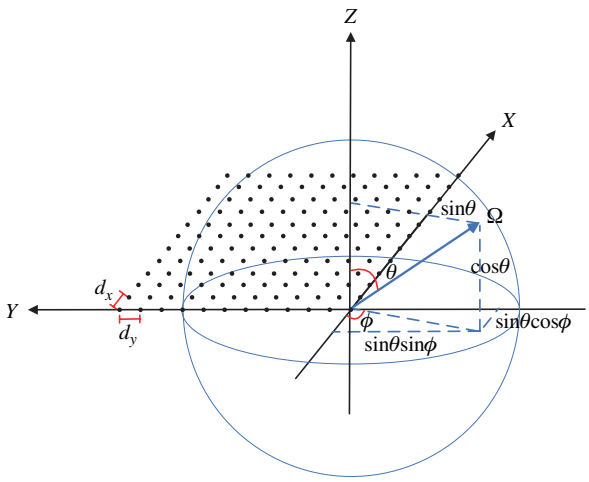

Figure 1 (Color online) Spherical coordinate and uniform planar array configuration.

1) A FD-SAGE algorithm is introduced and extended to extract 3D angle information accurately. The performance is verified in both synthetic and real environments.

2) Channel measurements at 16, 28, and 38 GHz using large horizontal planar arrays are conducted in a typical indoor office environment. Statistical properties such as averaged PDP (APDP), PDP, PAAP, and PEAP are investigated to observe typical characteristics such as the large path attenuation, spherical wavefront, and non-stationarity characteristics of mmWave massive MIMO channels.

3) SCCFs along different dimensions of the large array and at different frequency bands are compared and exhibit significant variances.

The remainder of this paper is organized as follows. System model and the high resolution 3D FD-SAGE algorithm are introduced in Section 2. In Section 3, measurement environment and setups are described. Simulation results and analysis are given in Section 4. Finally, conclusions are drawn in Section 5.

2 System model and 3D FD-SAGE algorithm

2.1 System model

In a time invariant environment, MPCs arrive at the Rx antenna element with different complex amplitudes α, delays τ, AAoA ϕ_R, EAoA θ_R, AAoD ϕ_T, and EAoD θ_T. The channel impulse response (CIR) at one antenna element can be represented by summing L MPCs up [7], e.g.,

$$h(\tau) = \sum_{l=1}^{L} \alpha_l \delta(\tau - \tau_l)\delta(\boldsymbol{\Omega}_T - \boldsymbol{\Omega}_{T,l})\delta(\boldsymbol{\Omega}_R - \boldsymbol{\Omega}_{R,l}) + w(t), \tag{1}$$

where $\delta(\cdot)$ is the Dirac delta function, $w(t)$ is the standard zero-mean complex white Gaussian noise, α_l, τ_l, $\boldsymbol{\Omega}_{T,l}$, and $\boldsymbol{\Omega}_{R,l}$ are the complex amplitude, delay, AoD, and AoA of the lth path, respectively. It is worth mentioning that $\boldsymbol{\Omega}_{T/R}$ is a unit vector uniquely determined by azimuth angle $\phi_{T/R}$ and elevation angle $\theta_{T/R}$, as shown in Figure 1. Taking the impinging wave as an example, the direction of the arrival wave Ω_R can be expressed in spherical coordinate, i.e.,

$$\boldsymbol{\Omega}_R = e(\phi_R, \theta_R) = [\cos(\phi_R)\sin(\theta_R), \sin(\phi_R)\sin(\theta_R), \cos(\theta_R)]^{\mathrm{T}}, \quad (\phi_R, \theta_R) \in [0, 2\pi) \times [0, \pi], \tag{2}$$

where $[\cdot]^{\mathrm{T}}$ denotes the transpose operator.

Assuming a MIMO system consisting of M transmitter (Tx) and N Rx antennas, the channel transfer function (CTF) can be represented as [9]

$$\boldsymbol{H}(f) = \sum_{l=1}^{L} \alpha_l \boldsymbol{c}_2(\boldsymbol{\Omega}_{R,l})\boldsymbol{c}_1^{\mathrm{T}}(\boldsymbol{\Omega}_{T,l})\mathrm{e}^{-\mathrm{j}2\pi f \tau_l} + \boldsymbol{W}(f). \tag{3}$$

At each frequency f, $\boldsymbol{H}(f)$ is a N-by-M matrix, and $\boldsymbol{W}(f)$ is the complex white Gaussian noise. Steering vectors $\boldsymbol{c}_1(\boldsymbol{\Omega}_T)$ and $\boldsymbol{c}_2(\boldsymbol{\Omega}_R)$ represent the response of the arrays to a wave emitting/impinging from directions $\boldsymbol{\Omega}_T$ and $\boldsymbol{\Omega}_R$, respectively, and can be expressed as [16]

$$\boldsymbol{c}_1(\boldsymbol{\Omega}_T) = f_{T,m}(\boldsymbol{\Omega}_T)\exp\{\mathrm{j}2\pi\lambda^{-1}\langle e(\boldsymbol{\Omega}_T), \boldsymbol{r}_{T,m}\rangle\}, \quad m = 1, \ldots, M, \tag{4}$$

$$\boldsymbol{c}_2(\boldsymbol{\Omega}_R) = f_{R,n}(\boldsymbol{\Omega}_R)\exp\{\mathrm{j}2\pi\lambda^{-1}\langle e(\boldsymbol{\Omega}_R), \boldsymbol{r}_{R,n}\rangle\}, \quad n = 1, \ldots, N, \tag{5}$$

where λ, $f_{T,m}(\boldsymbol{\Omega}_T)$ and $f_{R,n}(\boldsymbol{\Omega}_R)$, $\boldsymbol{r}_{T,m}$ and $\boldsymbol{r}_{R,n}$ denote the wavelength, complex antenna radiation pattern of Tx and Rx antennas, and Tx/Rx antenna location vectors, respectively. For a uniformly horizontal planar array, the inner product between the unit vector $e(\boldsymbol{\Omega})$ and location vector $\boldsymbol{r} = (r_x, r_y, 0)$ is calculated as

$$\langle e(\boldsymbol{\Omega}), \boldsymbol{r}\rangle = [r_x, r_y, 0][\cos(\phi)\sin(\theta), \sin(\phi)\sin(\theta), \cos(\theta)]^{\mathrm{T}}. \tag{6}$$

As depicted in Figure 1, d_x/d_y is the equi-distance between two adjacent antenna elements in x/y-axis of the large array.

Further considering K frequency bins, the CTF matrix can be expressed as [10]

$$\boldsymbol{H}(k) = \sum_{l=1}^{L} \boldsymbol{s}(k; \boldsymbol{\Theta}_l) + \boldsymbol{W}(k), \quad 1 \leqslant k \leqslant K, \tag{7}$$

where $\boldsymbol{\Theta}_l = [\tau_l, \boldsymbol{\Omega}_{T,l}, \boldsymbol{\Omega}_{R,l}, \alpha_l]$ contains all the parameters of the lth path, $\boldsymbol{s}(k; \boldsymbol{\Theta}_l) = \alpha_l \boldsymbol{c}_2(\boldsymbol{\Omega}_{R,l})\boldsymbol{c}_1^{\mathrm{T}}(\boldsymbol{\Omega}_{T,l})$ $\mathrm{e}^{-\mathrm{j}2\pi f_k \tau_l}$ is the component contributed by the lth path [7], and $\boldsymbol{W}(k)$ is the noise matrix.

2.2 3D FD-SAGE algorithm

SAGE algorithm is an extension of EM algorithm by dividing all the parameters into several subsets in the maximization step. Complete data (unobservable) and incomplete data (observable) are two key notions in the SAGE algorithm and the choice of complete data should guarantee the complexity and convergence rate of parameter estimation procedure. As specified in [16], the natural choice of complete data given below leads to a surprisingly simple scheme,

$$\boldsymbol{X}_l(k) = \boldsymbol{s}(k; \boldsymbol{\Theta}_l) + \boldsymbol{W}(k). \tag{8}$$

The incomplete data is expressed as $\boldsymbol{H}(k) = \sum_{l=1}^{L} \boldsymbol{X}_l(k)$. If $\{\boldsymbol{X}_l(k),\ l = 1, \ldots, L\}$ is known, the parameters of each path $\{\boldsymbol{\Theta}_l,\ l = 1, \ldots, L\}$ can be estimated by searching parameters that maximize the maximum likelihood estimation (MLE) functions. However, as $\boldsymbol{X}_l(k)$ is unknown in practical, it can be obtained by subtracting the contributions of all the paths except the lth path from $\boldsymbol{H}(k)$,

$$\hat{\boldsymbol{X}}_l(k; \hat{\boldsymbol{\Theta}}'_l) = \mathrm{E}[\boldsymbol{X}_l(k)|\boldsymbol{H}(k), \hat{\boldsymbol{\Theta}}'_{l'}] = \boldsymbol{H}(k) - \sum_{l'=1, l' \neq l}^{L} \boldsymbol{s}(k; \hat{\boldsymbol{\Theta}}'_{l'}). \tag{9}$$

Eq. (9) represents the "E"—expectation step of the SAGE algorithm using parallel interference cancellation (PIC) method. Here, $\hat{\boldsymbol{\Theta}}'_{l'}$ denotes the initial assumption or previous estimation of the l'th path parameters.

Given the complete data acquired above, parameters of MPCs can be derived by searching the values that can maximize the cost function [7], which is given by

$$\mathrm{z} = \boldsymbol{c}_2^{\mathrm{H}}(\boldsymbol{\Omega}_R) \sum_{k=1}^{K} \mathrm{e}^{\mathrm{j}2\pi f_k \tau} \hat{\boldsymbol{X}}_l(k; \hat{\boldsymbol{\Theta}}'_l) \boldsymbol{c}_1^*(\boldsymbol{\Omega}_T), \tag{10}$$

where $[\cdot]^{\mathrm{H}}$ and $[\cdot]^*$ denote Hermitian transpose operator and complex conjugation. In the 3D FD-SAGE algorithm, parameters are divided into three sub-sets: $\{\tau_l, \alpha_l\}$, $\{\boldsymbol{\Omega}_{T,l}, \alpha_l\}$, and $\{\boldsymbol{\Omega}_{R,l}, \alpha_l\}$, which are consecutively searched in each iteration step [16],

$$\hat{\tau}''_l = \arg\max_{\tau}\{|\mathrm{z}(\tau, \hat{\boldsymbol{\Omega}}'_{T,l}, \hat{\boldsymbol{\Omega}}'_{R,l}; \hat{\boldsymbol{X}}_l(k; \hat{\boldsymbol{\Theta}}'_l))|\}, \tag{11}$$

$$\hat{\boldsymbol{\Omega}}''_{T,l} = [\hat{\phi}''_{T,l}, \hat{\theta}''_{T,l}] = \arg\max_{\boldsymbol{\Omega}_T}\{|\mathrm{z}(\hat{\tau}''_l, \boldsymbol{\Omega}_T, \hat{\boldsymbol{\Omega}}'_{R,l}; \hat{\boldsymbol{X}}_l(k; \hat{\boldsymbol{\Theta}}'_l))|\}, \tag{12}$$

$$\hat{\boldsymbol{\Omega}}''_{R,l} = [\hat{\phi}''_{R,l}, \hat{\theta}''_{R,l}] = \arg\max_{\boldsymbol{\Omega}_R}\{|\mathrm{z}(\hat{\tau}''_l, \hat{\boldsymbol{\Omega}}''_{T,l}, \boldsymbol{\Omega}_R; \hat{\boldsymbol{X}}_l(k; \hat{\boldsymbol{\Theta}}'_l))|\}, \tag{13}$$

$$\hat{\alpha}''_l = \frac{1}{MNK}\mathrm{z}(\hat{\tau}''_l, \hat{\boldsymbol{\Omega}}''_{T,l}, \hat{\boldsymbol{\Omega}}''_{R,l}; \hat{\boldsymbol{X}}_l(k; \hat{\boldsymbol{\Theta}}'_l)). \tag{14}$$

Eqs. (11)–(14) are referred to as the "M"—maximization step. Iteratively carrying out the "E" and "M" steps, a sequence of estimates can be generated until the cost function converges to a stationary point.

The initialization of each path parameters is also influential to the convergence rate of the iteration technique. Successive interference cancellation (SIC) method orders all the estimated waves in descending order according to the path power. It can avoid the inaccuracy estimation of weak MPCs caused by strong MPCs. With SIC method, "E" step in (9) can be rewritten as

$$\hat{\boldsymbol{X}}_l(k; \hat{\boldsymbol{\theta}}'_l) = \boldsymbol{H}(k) - \sum_{l'=1}^{l-1} \boldsymbol{s}(k; \hat{\boldsymbol{\Theta}}'_{l'}). \tag{15}$$

Within the SIC initialization procedure, Eqs. (11)–(13) can be replaced by (16)–(18) with pre-initial setting $\hat{\boldsymbol{\Theta}}' = [0, \ldots, 0]$ for each path. The initialization for all paths is consecutively carried out similar to the SAGE iteration procedure. Note that in the initialization procedure, we choose two-dimensional grid search scheme to estimate departure and incidence angles rather than one-dimensional search scheme, because the former would provide more accurate estimation of the direction information [8].

$$\hat{\tau}''_l = \arg\max_{\tau}\left\{\sum_{m=1}^{M}\sum_{n=1}^{N}\left|\sum_{k=1}^{K}\mathrm{e}^{\mathrm{j}2\pi f_k \tau}\boldsymbol{X}_{l,n,m}(k; \hat{\boldsymbol{\Theta}}''_l)\right|^2\right\}, \tag{16}$$

$$\hat{\boldsymbol{\Omega}}''_{T,l} = \arg\max_{\boldsymbol{\Omega}_T}\left\{\sum_{n=1}^{N}\left|\sum_{k=1}^{K}\mathrm{e}^{\mathrm{j}2\pi f_k \hat{\tau}''_l}\boldsymbol{X}_{l,n,\cdot}(k; \hat{\boldsymbol{\Theta}}''_l)\boldsymbol{c}_1^*(\boldsymbol{\Omega}_T)\right|^2\right\}, \tag{17}$$

$$\hat{\boldsymbol{\Omega}}''_{R,l} = \arg\max_{\boldsymbol{\Omega}_R}\left\{\sum_{m=1}^{M}\left|\boldsymbol{c}_2^{\mathrm{H}}(\boldsymbol{\Omega}_R)\sum_{k=1}^{K}\mathrm{e}^{\mathrm{j}2\pi f_k \hat{\tau}''_l}\boldsymbol{X}_{l,\cdot,m}(k; \hat{\boldsymbol{\Theta}}''_l)\right|^2\right\}, \tag{18}$$

where $\boldsymbol{X}_{l,n,\cdot}(k; \hat{\boldsymbol{\Theta}}''_l)$ and $\boldsymbol{X}_{l,\cdot,m}(k; \hat{\boldsymbol{\Theta}}''_l)$ are the nth row and mth column of the lth path complete data, respectively.

2.3 Channel statistical properties

In this paper, channel statistics such as APDP, PAAP, PEAP, and SCCF are investigated. The calculations can be expressed as [15]

$$\mathrm{APDP} = \frac{1}{N_x N_y}\sum_{i=1}^{N_x}\sum_{j=1}^{N_y}|h_{i,j}(k)|^2, \quad 1 \leqslant k \leqslant K, \tag{19}$$

$$\mathrm{PAAP} = \sum_{l=1}^{L}|\alpha_l|^2\delta(\phi - \phi_{R,l}), \tag{20}$$

$$\mathrm{PEAP} = \sum_{l=1}^{L}|\alpha_l|^2\delta(\theta - \theta_{R,l}), \tag{21}$$

$$\rho_{h_{i,j},h_{i',j'}} = \frac{\mathrm{E}\left\{(h_{i,j} - \bar{h}_{i,j})(h_{i',j'} - \bar{h}_{i',j'})\right\}}{\sqrt{\mathrm{E}\left\{(h_{i,j} - \bar{h}_{i,j})^2(h_{i',j'} - \bar{h}_{i',j'})^2\right\}}}. \tag{22}$$

Here, i and i', j and j' are the antenna indices in x- and y- axes of a planar array, respectively. Horizontal planar array size is $N_x \times N_y$. The CIR $h_{(\cdot)}$ can be obtained by the discrete inverse Fourier transform (FT) operation of $\boldsymbol{H}_{(\cdot)}$ and $\bar{h}_{(\cdot)}$ is the mean value.

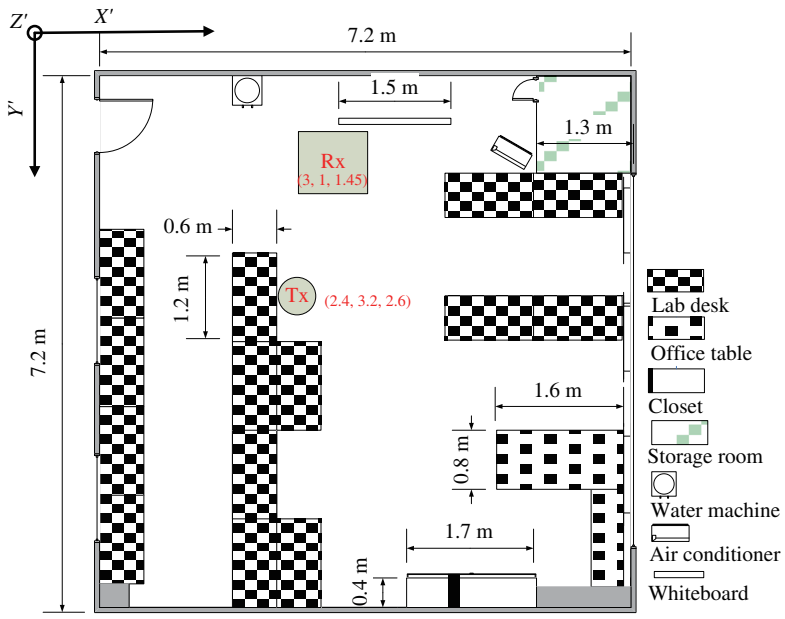

Figure 2 (Color online) Layout of the indoor office.

Table 1 Measurement setups

Center frequency, f_c (GHz)	16	28	38
Wavelength, λ (mm)	19	11	8
Bandwidth, B (GHz)	2	4	4
Sweeping points, K	401	801	801
Rx array elements	76×76	91×91	121×121
Array size (mm^2)	600×600	360×360	360×360
Antenna spacing step, $d_x = d_y$ (mm)	8	4	3
Rayleigh distance, R (m)	75.8	47.1	64.8

3 Measurement description

To investigate the new propagation characteristics of indoor mmWave massive MIMO channels, channel measurements at 16, 28, and 38 GHz bands in a typical office environment using the Keysight N5227A VNA are conducted. The vertically polarized biconical antenna working at 3–40 GHz bands is connected to Port 2 of the VNA at the Rx side, while three horn antennas covering 15–22, 22–33, and 33–50 GHz bands, respectively, are successively connected to Port 1 at the Tx side [15]. The layout of the office is shown in Figure 2. It is furnished with chairs, desks, computers, and electronic devices. The size of the office is 7.2 m × 7.2 m × 3 m. The locations of Tx antenna and Rx array center are $(3, 1, 1.45)$ and $(2.4, 3.2, 2.6)$, respectively. Note that close to the Rx array, there is a whiteboard with an area of 1.5 m^2. Channel measurements using sweeping frequency method is usually time consuming, and thus, the environment is kept quasi-static during measurements. Detailed system setups of three frequency bands can be found in Table 1.

Rayleigh distance is one key factor that can be used to distinguish near field region and far field region of the radiation field of antennas. It can be calculated as $R = 2D^2/\lambda$, where D is the maximum aperture dimension of the antenna array. If the Tx-Rx distance is beyond the Rayleigh distance, planar wavefront assumption is held. Otherwise, spherical wavefront must be considered. In massive MIMO channel measurements, Rayleigh distance calculated for a large antenna array is essential to judge whether the Tx and Rx are within the near field region of each other or not. Thus, the Rayleigh distances of three frequency bands with different Rx array sizes are given in Table 1. Figure 3 gives clear configuration

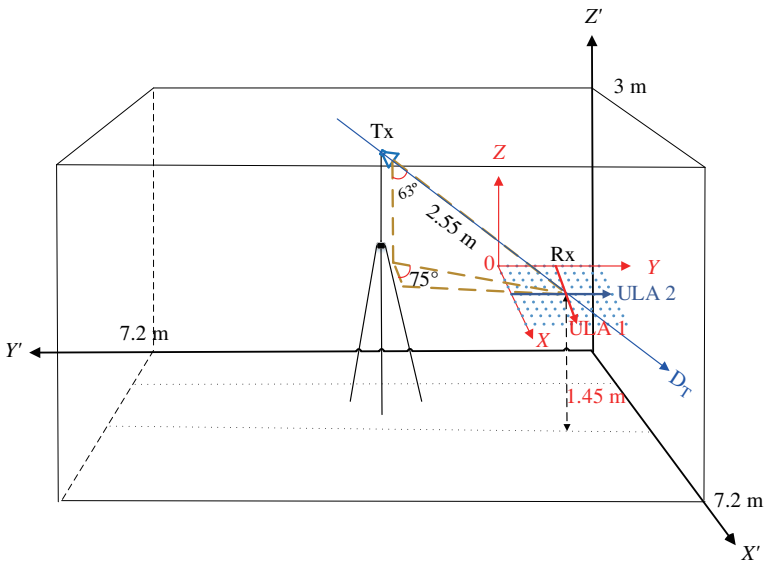

Figure 3 (Color online) Configurations of the Tx and Rx array.

of the Tx and Rx virtual array. A 10 dBi horn antenna is placed on a tripod at the Tx side. The omni-directional Rx antenna is placed on a 3D positioner and moved to form a large virtual horizontal uniformly planar array. The Tx-Rx distance is 2.55 m and Tx horn antenna is directed towards the center of the Rx array. Based on the line Tx-D_T line shown in Figure 3, relative angles of Tx pointing direction to ULAs 1 and 2 can be calculated. The azimuth angle deviations are 65° and −15° for ULA 1 and 2, respectively. The elevation angle deviations are both 27°. Specific positions of antenna elements for the Rx array can be symbolized by their x-y-z coordinates.

4 Simulation and measurement results

4.1 Performance of the 3D FD-SAGE algorithm

As required by broadband transmission at mmWave frequency bands, the wideband channel sounder has higher delay resolution than conventional channel measurement. As listed in Table 1, the delay resolutions are 0.5 ns and 0.25 ns for channel measurements with bandwidths set to 2 GHz and 4 GHz, respectively. Furthermore, the usage of large array can achieve better angular resolutions than conventional MIMO array. Thus, high resolution channel parameter estimation algorithms designed for broad bandwidth and large array are used to extract parameters of abundant MPCs. In this part, performance of the proposed 3D FD-SAGE algorithm is analyzed in both synthetic channel and real measurement environments.

In simulation environment, the array setups, path number, and the distributions of the parameters of MPCs are given in Table 2. In accordance with the measurement setups, the bandwidth is assumed to be 4 GHz with 801 frequency sample points. The grid steps used to search delay and angle are set to 0.25 ns and 1°, respectively. Figure 4 shows a comparison of the estimated results with the simulation settings. The solid lines ended with stars represent the simulation settings and circles stand for estimated parameters of 20 MPCs. It is clear that the estimation results of delay, AAoA, and EAoA for each path match very well the corresponding simulation settings. The path gain can be calculated based on the estimated delay and angles according to (14). It also coincides with the simulation settings and is not shown here. The SAGE algorithm also shows high resolution capability to distinguish two closely spaced MPCs in both delay and angular domains. For example, the MPCs with the same delay can be isolated if they have different angles. This phenomenon is also verified in Figure 4.

To testify the performance of the algorithm in real environment, the channel measurement data at 38 GHz is used. As the proposed 3D FD-SAGE algorithm can only be used in the case of plane wavefront assumption, only a central square sub-array with 15×15 elements is chosen from the virtual planar array.

Table 2 Parameter settings

Parameter	Simulation setting
Tx/Rx antenna	Omni-directional
Rx array size	$3 \times 3 \times 3$ cube array
Number of paths, L	20
Amplitude, α	Complex Gaussian distribution, $\alpha \sim \mathcal{CN}(0, 1)$
Delay, τ (ns)	Exponential distribution, $\tau \sim \text{Exp}(3)$
AAoA, ϕ (°)	Uniform distribution in $[-180, 180]$
EAoA, θ (°)	Uniform distribution in $[0, 180]$

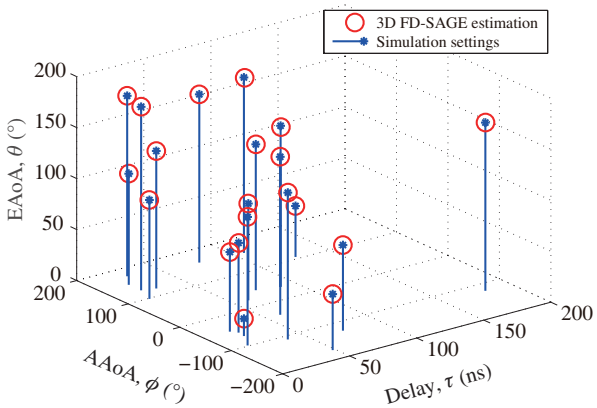

Figure 4 (Color online) Performance of the 3D FD-SAGE algorithm in a simulated environment (f_c = 38 GHz, B = 4 GHz, and $K = 801$).

Figure 5 shows the estimated delays, AAoAs, and power gains of 100 MPCs. Both colour and size of the circle are indicators of MPC power. Here, the number of MPCs are set to 100 in order to capture tantamount power of the real channel. As shown in Figure 5, a strong line-of-sight (LoS) component is extracted. The delay and AAoA of the LoS component are 7 ns and −17°, respectively, which are corresponding to the distance and relative position of Tx and Rx as indicated in Figure 3. By referring other strong paths back to the real environment, the correctness of estimation results can be verified.

4.2 Characteristics analysis of mmWave massive MIMO channels

For the convenience of further channel characteristic analysis over the array, two ULAs and five 15×15 square planar arrays are selected among the large array. As the array elements and sizes are different for the measured three frequency bands, here we take Rx array configuration at 38 GHz as an example. The selected sub-arrays are indicated in Figure 6. The two ULAs are selected to be parallel to the x- and y-dimensions of the planar array, and cross at the center of the planar array.

4.2.1 *Delay and angle variations in massive array*

To observe how the delay and incidence angle change within the large array, the channel PDPs of two ULAs and the channel PAAPs and PEAPs of five sub-arrays are compared. The PAAPs and PEAPs are calculated from the estimated parameters of five sub-arrays according to (20) and (21).

Figure 7 shows the PDPs calculated with measurement data at 38 GHz. In Figure 7(a), we can see that the delays of strong MPCs among different antenna elements in the ULA along x-axis have not shown significant variance. However, in Figure 7(b) the delay of the LoS component along y-axis increase from 6.75 ns to 7.75 ns. This is mainly caused by the increased distance between Tx antenna and Rx antenna elements along y-axis. Furthermore, some components with relative strong powers disappear along the ULAs. For example, in Figure 7(b), the powers of MPCs with delay around 33 ns is larger

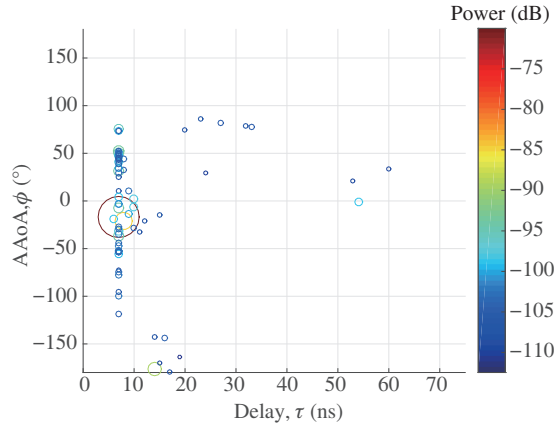

Figure 5 (Color online) MPCs estimated using the proposed 3D FD-SAGE algorithm in a real environment (f_c = 38 GHz, B = 4 GHz, and K = 801).

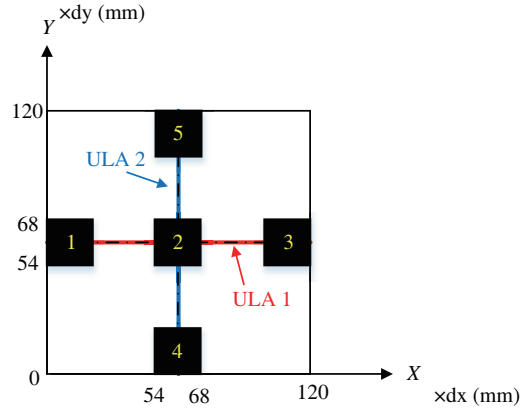

Figure 6 (Color online) Sub-arrays selected in the Rx array.

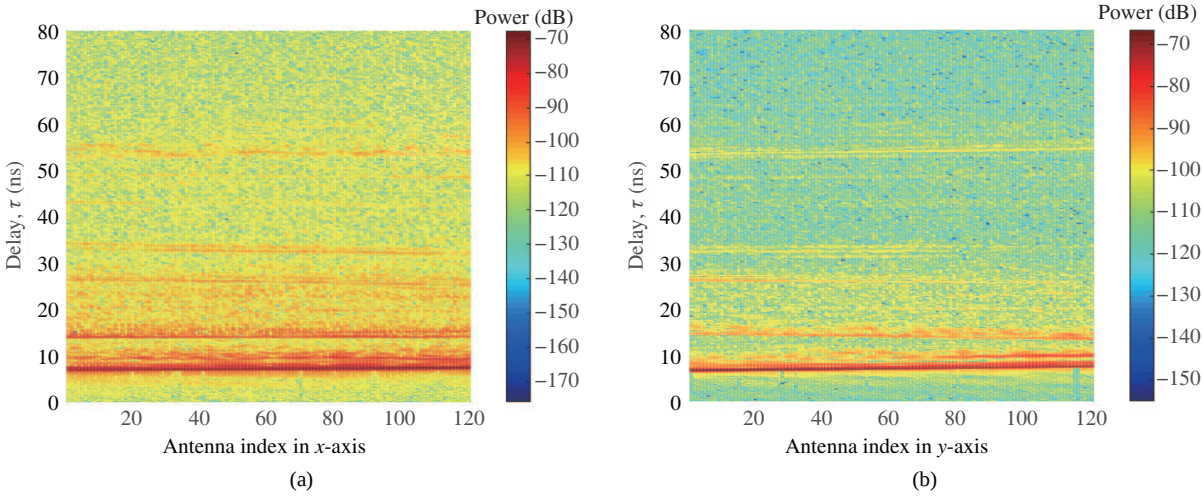

Figure 7 (Color online) Delay shifts along (a) ULA 1 and (b) ULA 2 (f_c = 38 GHz, B = 4 GHz, and K = 801).

than −100 dB for antenna elements with index smaller than 80 in x-axis. But the powers decrease to −118 dB for antennas with index larger than 80. This can be interpreted as those MPCs are hidden or blocked for part of the antenna elements, and can be modeled by a birth-death process.

We use the 3D FD-SAGE algorithm to estimate channel parameters for the five square sub-arrays 1–5. Then, according to (20) and (21), the PAAPs for sub-arrays 1–3 and PEAPs for sub-arrays 2, 4, and 5 are calculated to see the variations of AAoAs and EAoAs clearly. As shown in Figure 8, the 5 strongest MPCs are extracted. In Figure 8(a), the AAoAs of stronger MPCs shift from −13° to −23° for sub-arrays from 1 to 3. This represents the relative position changing between Tx antenna and each sub-array. Likewise, the EAoAs of stronger MPCs shift from 65° to 60° for sub-arrays from 4 to 2 and further to 5, as shown in Figure 8(b). Along with the angle shift, the power fluctuation is also found among the selected arrays.

4.2.2 *SCCFs along different dimensions of a planar array*

As discussed in Figures 7 and 8, the parameters of MPCs being observed along different dimensions of the large Rx array are quite different. In this part, we further analyze the SCCF variants over different dimensions of the large Rx array. The channel measurement data at 38 GHz is chosen, and the SCCFs are calculated according to (22). In Figure 9, the spatial correlation coefficients between the channels of two distinct elements along the positive direction of x-axis and y-axis are shown, respectively. It is

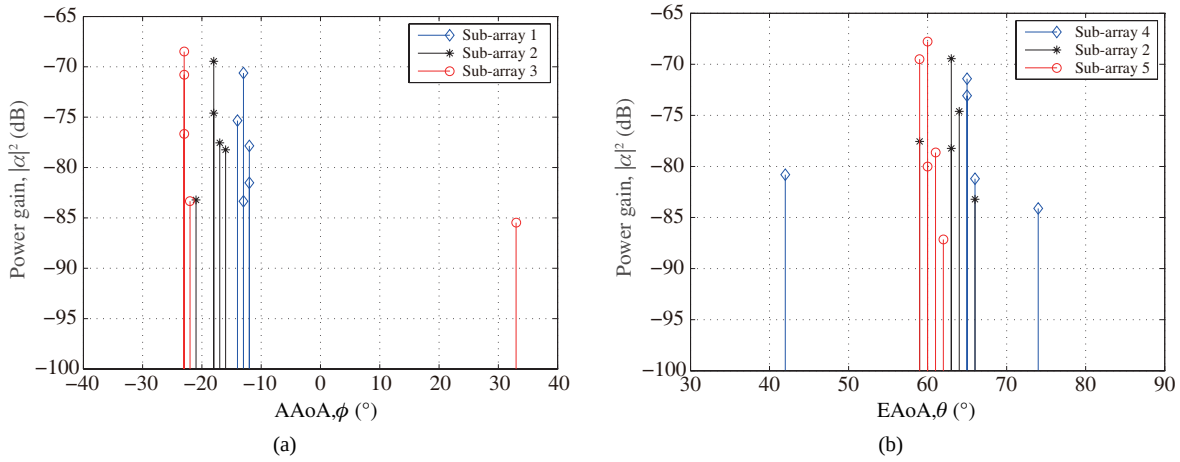

Figure 8 (Color online) Angle shifts along different directions of the planar array. (a) AAoA shifts among sub-arrays 1–3 and (b) EAoA shifts among sub-arrays 4, 2, and 5 ($f_c = 38$ GHz, $B = 4$ GHz, and $K = 801$).

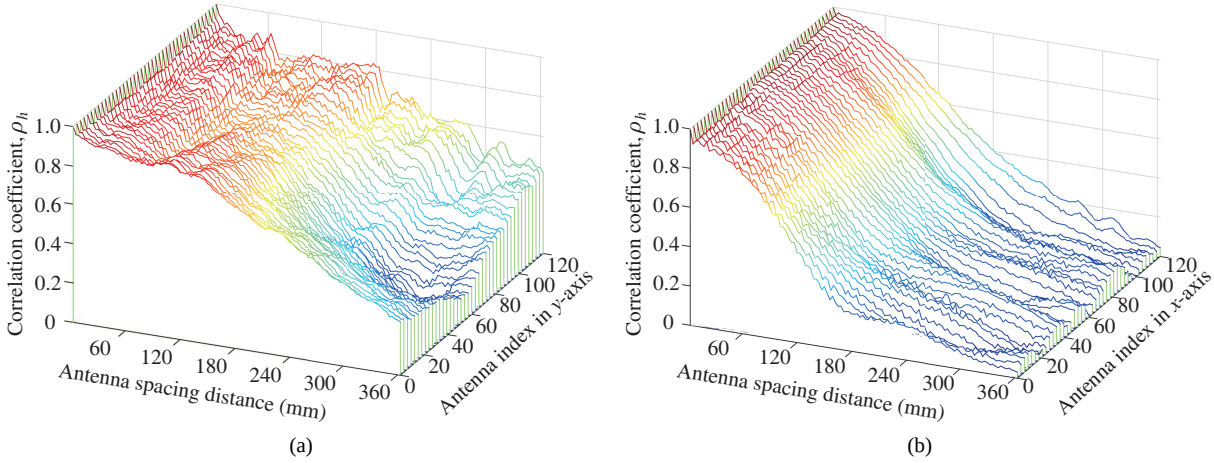

Figure 9 (Color online) SCCFs along different directions of the planar array. (a) Along x-axis and (b) along y-aixs ($f_c = 38$ GHz, $B = 4$ GHz, and $K = 801$).

clear to see that the correlation coefficients calculated toward positive direction of the x-axis decrease gradually but higher than 0.2, while they decrease rapidly and approach 0 toward the y-axis. This is caused by the different distances and angles between the Tx and those ULAs parallel to x-axis and y-axis, respectively [4].

4.2.3 *Comparison of channel characteristics at different frequency bands*

Considering that the attenuation at mmWave band are significantly compared with sub-6 GHz band, in this part, we focus on studying the channel characteristics at three frequency bands. We select measurement data from three 15×15 central square sub-arrays at 16, 28, and 38 GHz, respectively, and compare the APDPs calculated according to (19). As shown in Figure 10, the power difference of the LoS components between 16 and 28 GHz is 3.6 dB, while it is 3.12 dB between 28 and 38 GHz. For MPCs with large delays, for example around 55 ns, we can draw the same conclusion. It is also shown that channels at these three bands share the similar delay distributions except for the difference in power gains.

In Figure 11, SCCFs are calculated by using the measurement data of the selected two ULAs for three frequency bands. It is shown in Figure 11(a) that the SCCF calculated along ULA 1 at 38 GHz decreases faster than those at 28 and 16 GHz bands. While in Figure 11(b), the SCCF calculated along ULA 2 at 28 GHz decreases faster than those at 38 and 16 GHz bands. In both figures, the SCCFs at 16 GHz have

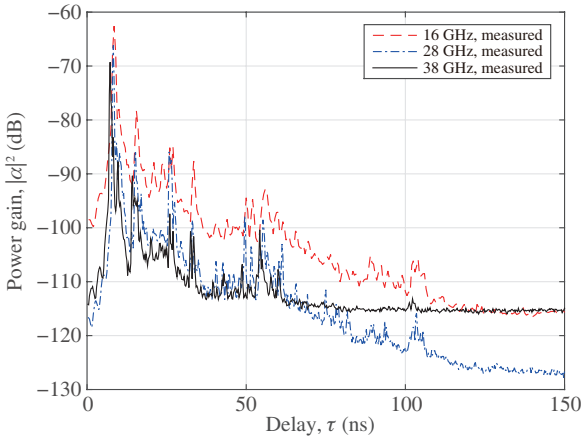

Figure 10 (Color online) Comparison of APDPs at three frequency bands.

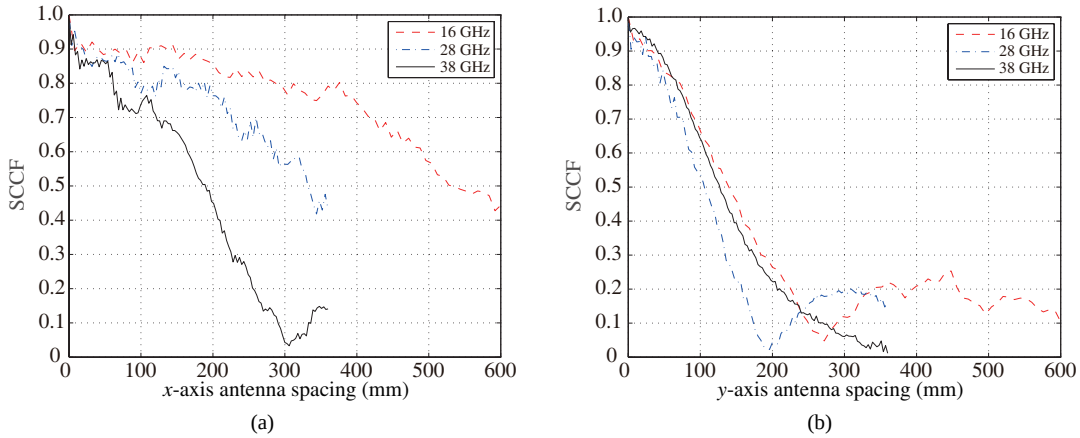

Figure 11 (Color online) Comparison of SCCFs at three frequency bands. (a) Along ULA 1 and (b) along ULA 2.

the slowest decreasing rate. The dramatic change of SCCFs along two dimensions of the planar array at 28 GHz band may attribute to the different mmWave propagation characteristics [14]. Comparing Figures 11 (a) and (b), we can see that the difference of SCCFs along x- and y- axes for 38 GHz is less significant than those at 16 and 28 GHz bands.

5 Conclusion

In this paper, we have presented the channel measurements carried out in an indoor office environment using large virtual horizontal planar array at three mmWave frequency bands, i.e., 16, 28, and 38 GHz. A 3D FD-SAGE algorithm has been proposed and verified in both synthetic and real environments, and used to extract MPC parameters from channel measurement data. With the estimated parameters, the AAoA and EAoA shifts and power variations at several sub-arrays have been shown. Obvious path delay shift and cluster birth-death phenomenon along two ULAs of the large array have also been observed. The SCCFs have been calculated along two directions of the planar array and at three frequency bands, and have shown significant variations. By comparing the SCCFs at three frequency bands, we have also found that the SCCF along y-axis at 28 GHz decreases even faster than those at 16 and 38 GHz. It has been demonstrated that the SCCFs can be affected by the operating frequency bands as well as the relative angle between Tx pointing direction and Rx array. Those characteristics should be considered in future channel measurements and modeling, and will help with the antenna configuration and orientation when deploying a large array.

Acknowledgements This work was supported by EU H2020 ITN 5G Wireless Project (Grant No. 641985), EU H2020 RISE TESTBED Project (Grant No. 734325), EU FP7 QUICK Project (Grant No. PIRSES-GA-2013-612652), EPSRC TOUCAN project (Grant No. EP/L020009/1), National Natural Science Foundation of China (Grant Nos. 61210002, 61371110), Xinwei Telecom Technology Inc. (Grant No. 11131701), and Fundamental Research Funds of Shandong University (Grant No. 2017JC009).

Conflict of interest The authors declare that they have no conflict of interest.

References

1 Ge X H, Chen J Q, Wang C X, et al. 5G green cellular networks considering power allocation schemes. Sci China Inf Sci, 2016, 59: 022308
2 Wang C X, Haider F, Gao X Q, et al. Cellular architecture and key technologies for 5G wireless communication networks. IEEE Commun Mag, 2014, 52: 122–130
3 Gustafson C, Haneda K, Wyne S, et al. On mmWave multipath clustering and channel modeling. IEEE Trans Antenn Propag, 2013, 62: 1445–1455
4 Wu S B, Wang C X, Aggoune H, et al. A non-stationary 3D wideband twin-cluster model for 5G massive MIMO channels. IEEE J Sel Areas Commun, 2014, 32: 1207–1218
5 Wang C X, Wu S B, Bai L, et al. Recent advances and future challenges for massive MIMO channel measurements and models. Sci China Inf Sci, 2016, 59: 021301
6 Ayanoglu E, Heydari P, Capolino F. Millimeter-wave massive MIMO: the next wireless revolution? IEEE Commun Mag, 2014, 52: 56–62
7 Fleury B H, Tschudin M, Heddergott R, et al. Channel parameter estimation in mobile radio environments using the SAGE algorithm. IEEE J Sel Areas Commun, 1999, 17: 434–450
8 Fleury B H, Yin X, Rohbrandt K G, et al. Performance of a high-resolution scheme for joint estimation of delay and bidirection dispersion in the radio channel. In: Proceedings of IEEE Vehicular Technology Conference, Birmingham, 2002. 522–526
9 Chong C C, Laurenson D I, Tan C M, et al. Joint detection-estimation of directional channel parameters using the 2-D frequency domain SAGE algorithm with serial interference cancellation. In: Proceedings of IEEE International Conference on Communications, New York, 2002. 906–910
10 Matthaiou M, Laurenson D I, Razavi-Ghods N, et al. Characterization of an indoor MIMO channel in frequency domain using the 3D-SAGE algorithm. In: Proceedings of IEEE International Conference on Communications, Glasgow, 2007. 5868–5872
11 Feng R, Huang J, Sun J, et al. Millimeter wave channel parameter estimation using a 3D frequency domain SAGE algorithm. In: Proceedings of 19th International Symposium on Wireless Personal Multimedia Communications, Shenzhen, 2016
12 Gao X, Edfors O, Rusek F, et al. Massive MIMO performance evaluation based on measured propagation data. IEEE Trans Wirel Commun, 2015, 14: 3899–3911
13 Payami S, Tufvesson F. Channel measurements and analysis for very large array systems at 2.6 GHz. In: Proceedings of 6th European Conference on Antennas and Propagation, Prague, 2012. 433–437
14 Rappaport T S, Sun S, Mayzus R, et al. Millimeter wave mobile communications for 5G cellular: it will work! IEEE Access, 2013, 1: 335–349
15 Huang J, Wang C X, Feng R, et al. Multi-frequency mmWave massive MIMO channel measurements and characterization for 5G wireless communication systems. IEEE J Sel Areas Commun, 2017, 35: 1591–1605
16 Fleury B H, Jourdan P, Stucki A. High-resolution channel parameter estimation for MIMO applications using the SAGE algorithm. In: Proceedings of IEEE Broadband Communications, Zurich, 2002. 30-1–30-9